Coherent evolution of potential vorticity anomalies associated with deep moist convection

RMetS
Royal Meteorological Society

Coherent evolution of potential vorticity anomalies associated with deep moist convection

C. Weijenborg,[a]* J. M. Chagnon,[b] P. Friederichs,[a] S. L. Gray[c] and A. Hense[a]
[a]*Meteorological Institute, University of Bonn, Germany*
[b]*Department of Earth, Ocean, and Atmospheric Science, Florida State University, Tallahassee, USA*
[c]*Department of Meteorology, University of Reading, UK*

*Correspondence to: C. Weijenborg, Meteorological Institute, University of Bonn, Auf dem Hügel 20, 53121 Bonn, Germany. E-mail: cwborg@uni-bonn.de

Potential vorticity (PV) elegantly describes synoptic- and planetary-scale dynamics, but it has received less attention on smaller scales. On the convective scale, PV is characterised by dipoles associated with convective cells. We show that the PV dipoles are statistically significant and associated with statistically significant flow anomalies. Our hypothesis is that there is a coherent evolution of the PV dipoles. This hypothesis is tested by tracking convective cells in the non-hydrostatic COSMO-DE numerical weather prediction model during nine severe weather events. The 3135 convective cells used in this study are representative of deep moist convection over Western Europe in the COSMO-DE model. Composites of the evolution of convective cells are made, and differences between 'normal' and intense cells are discussed.

Even when averaging over 3135 cells during nine cases, a clear horizontal PV dipole pattern can be seen with associated flow anomalies. Compared to normal cells, intense cells (identified using PV, precipitation rate or vertical velocity) have a more monopole morphology, which resembles that of supercells. The statistically significant flow anomalies associated with the PV anomalies imply that the PV dipoles might be invertible in a statistical way.

Key Words: potential vorticity; deep moist convection; diabatic processes; meso-γ scale

Received 30 May 2016; Revised 14 December 2016; Accepted 15 January 2017; Published online in Wiley Online Library 24 April 2017

1. Introduction

Due to the huge impact on society, knowledge of extreme convective-weather events is crucial. Economic costs related to severe weather exceeded US$ 1.4 trillion for the 1980–2004 period (Mills, 2005). Most of the insured property losses (about 70%) are related to small-scale weather events (Mills, 2005). Improving the physical understanding and forecasting of extreme events in general, and specifically those associated with deep moist convection, is one of the major challenges in modern meteorology (Shapiro and Thorpe, 2004). A fundamental problem in forecasting deep moist convection and its dynamics is the intense interaction of processes acting on a large range of spatial and temporal scales. On the one hand, one has microphysical processes which play a role in building individual clouds and, on the other hand, convection can organize itself into systems up to a few hundred kilometres across. Another reason for the limited predictability of mesoscale phenomena is that the associated eddy lifetimes are much shorter than for their synoptic counterparts. In this study we examine the evolution of potential vorticity (PV) on the convective-weather scale motivated by the prior use of this diagnostic on the synoptic scale to aid dynamical understanding and its potential use as a control variable in data assimilation.

On synoptic to planetary scales, PV provides insightful conceptual models to describe midlatitude dynamics (e.g. Hoskins *et al.*, 1985; Haynes and McIntyre, 1987). This is mainly due to two useful properties of PV. First, it is materially conserved for frictionless and adiabatic flow. This allows PV to be interpreted as a dynamical tracer. Second, given a balance and suitable boundary conditions, a PV field can be inverted to derive standard meteorological quantities such as wind velocity and pressure (Hoskins *et al.*, 1985). For synoptic and larger scales, quasi-geostrophic (QG) balance is generally a good assumption (Holton, 2004). A positive QG PV anomaly is associated with cyclonic rotation and a negative QG PV anomaly is associated with anticyclonic rotation (e.g. Hoskins *et al.*, 1985; Hoskins, 1997). The static stability inside a positive QG PV anomaly is increased relative to the background state; inside a negative QG PV anomaly the static stability is reduced. Below and above a QG

PV anomaly, the static stability perturbation has the opposite sign to that inside the PV anomaly. Furthermore, PV is very useful in indicating the effects of diabatic heating on atmospheric dynamics (Grams *et al.*, 2011; Chagnon *et al.*, 2012). Diabatic warming on the (sub-)synoptic scale leads to a vertical dipole of PV (Raymond and Jiang, 1990). On smaller scales PV has received less attention. The studies of PV dynamics on the mesoscale mainly focus on idealized test cases of mesoscale convective vorticies (e.g. Raymond and Jiang, 1990; Davis and Weisman, 1994; Cram and Montgomery, 2002; Schumacher and Johnson, 2008; Conzemius and Montgomery, 2009), on mesoscale orographic PV anomalies (e.g. Aebischer and Schär, 1998; Schär *et al.*, 2003), and on PV along fronts (e.g. Malardel *et al.*, 1993; Appenzeller and Davies, 1996).

On the convective-weather scale (≈10 km in the horizontal), PV has not been studied extensively. The published literature on storm dynamics mainly focuses on idealized case-studies (e.g. Weisman and Klemp, 1982, 1984; Droegemeier *et al.*, 1993; McCaul and Weisman, 2001). These studies often investigate only a few 'ideal' convective cells. Moreover, such studies tend to be positively biased towards more intense cells, since they focus on severe convection such as supercells in the US Great Plains. In contrast, this study concentrates on real simulated cases which occurred in Western Europe where the synoptic and mesoscale environment is different. Due to its potential use in, e.g., data assimilation, a detailed analysis of the typical PV anomalies on the convective-weather scale for real cases is necessary. Advantages of studying PV instead of vorticity dynamics is a clearer relationship of PV dynamics to diabatic heating; moreover, in the PV budget equation, sources and sinks can be more easily attributed to a specific physical process.

On the convective-weather scale the PV field is dominated by horizontally oriented dipoles, created by diabatic heating (Figure 1). These convective-scale PV dipoles are created by the tilting of horizontal vorticity caused by storm-scale updraughts (e.g. Conzemius and Montgomery, 2009), analogous to the creation of a dipole of vertical vorticity around an updraught (Davies-Jones, 1984; Lilly, 1986). Chagnon and Gray (2009) found those PV dipoles in an environment with moderate vertical shear of the horizontal flow to be related to heating on the storm scale originating from heating by moist processes inside clouds. PV tendencies from latent heating require the gradient of heating to be oriented in the direction of a background vorticity vector. In the case of a mesoscale region of heating, the vertical gradient of heating is aligned with the planetary vorticity vector; the associated PV tendencies comprise a vertical dipole (e.g. Raymond and Jiang, 1990). In the case of a convective-scale region of heating, the PV tendencies are instead dominated by the action of a horizontal gradient of heating aligned with the horizontal vorticity associated with vertical shear of the horizontal wind components; the resulting PV tendencies comprise a horizontal dipole (Chagnon and Gray, 2009).

Inversion of PV anomalies provides information on the flow and thermodynamic variables from 'just' the PV distribution (and suitable boundary conditions). Thus the ability to invert convective-scale PV anomalies, as can be done for synoptic-scale QG PV anomalies, would be very useful. The barrier to the inversion of convective-scale PV anomalies is the requirement of a balance condition. Deep moist convection is very unsteady, therefore it is unlikely that the flow around the mesoscale dipoles is balanced in the sense of large-scale dynamics. However, Chagnon and Gray (2009) and Weijenborg *et al.* (2015) present two arguments for these dipoles being coherent. First, Chagnon and Gray (2009) suggested that the PV dipoles created by convection have a longer lifetime than the original updraught that generated the dipole. They argued that, although the PV dipole is created by the horizontal vorticity component due to the vertical wind shear of the horizontal wind, the vorticity is tilted almost immediately into the vertical. The diabatic PV is related to the integrated heating, therefore these dipoles are relatively persistent. This can lead to dipoles that survive after the original convective heating has vanished. Second, the adjustment time-scale is determined by the longest period gravity waves generated by the cloud forcing. A cloud-scale forcing only generates short-period waves having time-scales closer to a buoyancy period (e.g. Chagnon and Bannon, 2005). Chagnon and Gray (2009) estimated from simulations of a frontal zone using an idealized two-dimensional model that the time-scale of adjustment of latent to relative vorticity for cumulus-scale heating is approximately 0.5 h. This is shorter than the lifetime of an individual convective cell. The ratio of the estimated adjustment time to the lifetime of a cell is indicative of a coherent flow. Another argument for presuming coherency is that severe convective weather associated with rotating cells is often relatively long-lasting (e.g. supercells, which can last for several hours). Since the dipoles cannot be exactly balanced, PV inversion in the classical way on the convective-weather scale might be impossible. However, it still would be very useful to determine the general PV and flow anomalies associated with deep moist convection.

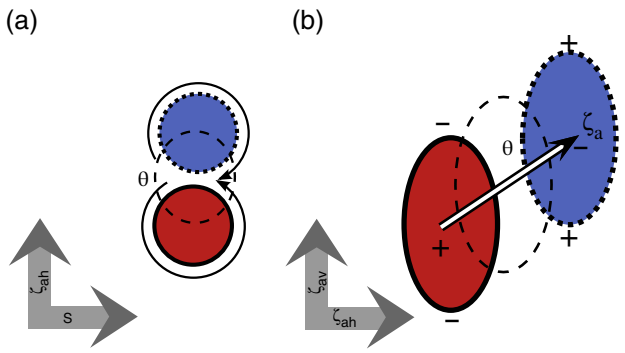

Figure 1. Schematic overview of PV dipoles generated due to convection, with diabatic perturbation indicated by the dashed black circle. The positive PV pole is indicated by the red circle and the negative PV anomaly is indicated by the dotted blue circle. Also indicated are the direction of the absolute vorticity vector $\boldsymbol{\zeta}_\mathbf{a}$, and its horizontal $\boldsymbol{\zeta}_\mathbf{ah}$ and vertical $\boldsymbol{\zeta}_\mathbf{av}$ components. (a) shows the horizontal cross-section, with PV dipoles created in the direction of absolute vorticity $\mathbf{k} \times \mathbf{S}$, with $\mathbf{S}$ the vertical wind shear. Storm relative wind velocities associated with the PV anomalies are indicated by black arrows. (b) shows the vertical cross-section along the direction of $\mathbf{k} \times \mathbf{S}$. Adapted from Weijenborg *et al.* (2015). [Colour figure can be viewed at wileyonlinelibrary.com].

To break with the traditional deterministic idea of balance, Hakim (2008) proposed a probabilistic PV inversion in which the conditional probability $f_{\mathbf{x}|\mathbf{q}}$ of the state vector $\mathbf{x}$ containing all variables of the full system (e.g. wind velocity, pressure) is related to the state vector $\mathbf{q}$ of some control variable (e.g. the PV). Using Bayes' theorem, this can be related to the conditional probability of the PV given the state vector $\mathbf{x}$ ($f_{\mathbf{q}|\mathbf{x}}$). The approach of Hakim (2008) might be useful on the convective-weather scale. This requires as a necessary precondition that coherent PV structure in and around convective cells does exist. We will test if such coherent structures show up consistently in a large sample of cells. Using the Hakim (2008) arguments implies that the estimated first moment of the conditional pdf is non-zero. Therefore testing for coherent PV structures is a necessary condition for probabilistic balance inversion defined by Hakim (2008). The actual balance and its inversion is beyond the scope of this article. Therefore we provide an estimate of the first moment (i.e. the mean) of the conditional probability $f_{\mathbf{q}|\mathbf{x}}$. We do this by characterizing the evolution of a sample of cells and the averaged PV anomalies associated with it. Composites using the EPS forecast data of the Consortium for Small-scale Modelling COSMO-DE numerical weather prediction (NWP) model for 5 and 22 June 2011 have shown that there is a consistent PV dipole associated with a convective updraught (Weijenborg *et al.*, 2015). In this study we also take the evolution of the PV anomalies into account, and we look at a broader spectrum of cases.

The purpose of this study is to investigate the coherent evolution of PV anomalies typically associated with (severe) deep

moist convection. Moreover, we want to test if this evolution differs for different synoptic environments. Therefore, we track convective cells for nine severe weather cases using the COSMO-DE NWP model. We generate convective cell composites over all nine severe weather cases and focus on the differences between intense and 'normal' convective cells.

This article is organized as follows. The tracking and compositing methodology is described in section 2. In section 3 we describe the convective background of the nine severe weather cases. Composites of diabatic heating, PV and flow anomalies are discussed in section 4. In section 5 the results and implications are discussed.

2. Methodology

To determine the coherent evolution of cells we make composites of typical cells at different stages of their evolution. To accomplish this, we track cells for nine severe weather cases, including the 5 and 22 June 2011 cases discussed in Weijenborg *et al.* (2015). Although the nine cases differ in their convective environment, we assume that there is a consistent PV dipole around a convective updraught independent of the convective background.

Tracking approaches have been previously used to characterize the typical evolution of cyclones in global NWP models (e.g. Murray and Simmonds, 1991; Zhang *et al.*, 2004; Pinto *et al.*, 2005; Rudeva and Gulev, 2007; Dacre and Gray, 2009), to track jet stream features (Limbach *et al.*, 2012), to track mesoscale convective systems (Arnaud *et al.*, 1992), and to track convective cells using radar data (e.g. Dixon and Wiener, 1993; Johnson *et al.*, 1998; Han *et al.*, 2009; Kyznarová and Novák, 2009; Moseley *et al.*, 2013; Stein *et al.*, 2015). On the convective-weather scale, using model data, tracking is a less-used technique, although it has recently received more attention (Plant, 2008; Caine *et al.*, 2013; Clark and Bullock, 2014; Stein *et al.*, 2015; Moseley *et al.*, 2016).

2.1. Selection of nine severe weather cases

The goal of this study is to characterize PV anomalies typically associated with (severe) deep moist convection. Moreover we want to investigate the variation of the PV anomalies in different synoptic environments. Thus, the weather cases are carefully chosen to be representative of severe weather over Germany. Selection criteria for these weather cases are:

- Severe weather observed over Germany; we select cases for which severe rain, severe wind gusts or significant hail was observed.
- A considerable amount of deep moist convection generated in the COSMO-DE model; since we are planning to make composites of fields around convective cells, we need a reasonably large sample of modelled convective cells.
- Reasonably skilful COSMO-DE model forecasts when verified against observations.
- Variation in synoptic and mesoscale situations associated with the severe weather events; for example, we want to select frontal cases (which are characterized by larger wind shear and strong large-scale frontal forcing) as well as local convective events. Furthermore, we want to select cases in which there is directional wind shear with height and cases in which the environmental wind is more unidirectional.

Based on these criteria, we select nine severe weather cases for which a reforecast is made (Table 1). Of these weather cases, four are from June 2011, two are from June and July 2012 and three are from June, July and August 2013. Examples of extreme weather observed during these cases can be found in Table 1. The choice of initiation of the forecast at 0000 or 1200 UTC is based on when the convection is dominant. For the cases on 5, 6 and 22 June 2011, convection took place mainly in the afternoon, while for the other cases it took place in the (early) evening. These nine cases have a good variability in background characteristics such as wind shear, convective available potential energy (CAPE) and storm relative helicity (SRH). These differences in convective characteristics are further discussed in section 3.

Table 1. Description of the extremes associated with the nine severe weather cases used in this study.

Case	Initialization time (UTC)	Extreme weather observed
5 June 2011	0000	68 mm in 2 h; Bonn, Germany.
6 June 2011	0000	73 mm in 24 h; Kirchdorf/Poel, Germany
22 June 2011	0000	Wind gusts $>120\,\mathrm{km\,h^{-1}}$; Baden-Württemberg
28 June 2011	1200	100 mm in 24 h; Herwijnen, Netherlands
30 June 2012	1200	Wind gusts $>100\,\mathrm{km\,h^{-1}}$; South Germany
28 July 2012	1200	78 mm in 6 h; Bahno, Czech Republic
20 June 2013	1200	101 mm in 24 h; Deuselbach, Germany. Wind gusts $156\,\mathrm{km\,h^{-1}}$; Andermatt-Gütsch, Switzerland
28 July 2013	1200	60 mm in 24 h; Feldberg, Schwarzwald, Germany
6 August 2013	1200	Wind gusts $140\,\mathrm{km\,h^{-1}}$; Wasserkuppe, Germany

For each of the cases, a single run reforecast was made, starting at the initialization time indicated.

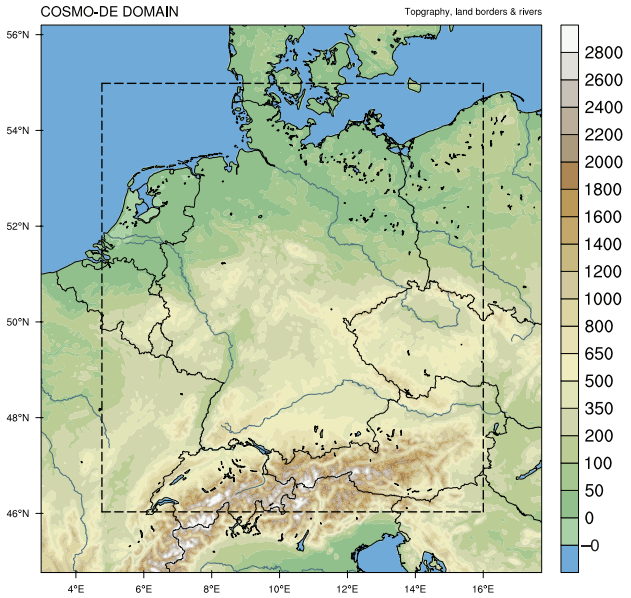

Figure 2. Domain and orography (m above sea level) of the COSMO-DE non-hydrostatic weather model. The dashed box indicates the inner domain of 321×361 grid points used in most calculations. [Colour figure can be viewed at wileyonlinelibrary.com].

2.2. Description of model

We use data from the limited-area non-hydrostatic weather prediction model COSMO-DE (Baldauf *et al.*, 2011) of the German Meteorological Service (DWD). The COSMO model is specially designed to operate on the meso-β and meso-γ scales (Schättler *et al.*, 2014). On these scales, deep moist convection is modelled explicitly by COSMO-DE. Therefore, we expect that severe convection phenomena, such as supercells and intense mesoscale convective systems, can be simulated directly.

The model domain is defined on an Arakawa-C grid and centred over Germany and surrounding countries (Figure 2). It contains 421×461 grid points in the horizontal with a grid spacing of 0.025° (approximately 2.8 km). The horizontal grid is rotated such that the equator of the model domain lies over Germany, yielding approximately constant grid spacing over

the whole domain. In the vertical, a modified hybrid height coordinate is used that follows the orography at the bottom levels and gradually flattens at higher levels. In total there are 50 vertical levels, with the first level at 10 m height and the top level at 21.5 km.

At the boundaries the model is driven by the larger-scale non-hydrostatic weather model COSMO-EU, which in turn is driven by the global hydrostatic weather model GME. Since the boundaries of the domain are heavily influenced by the dynamics of the large scale, all the plots in this article are for a subdomain, indicated by the dashed black lines in Figure 2. Here 50 grid points are removed at each lateral boundary.

2.3. Reforecast

Since convective cells have a lifetime of about an hour, it is essential to output data with a higher temporal resolution than the standard hourly output of COSMO-DE. To achieve this, reforecasts of nine severe weather events have been produced. We start each of these reforecasts from the deterministic COSMO-DE analysis. No further observational data are assimilated during the model run. All reforecasts are run for 24 h, and the output of the wind velocity components (u, v, w) and the PV are saved for all model levels. For these variables we choose to output every 2.5 min. Besides the high temporal resolution data, the standard output of COSMO-DE, including convective parameters such as CAPE and convective inhibition (CIN), is saved every 15 min.

2.4. Motivation for tracking the vertical velocity

Most of the published convection-tracking-based studies focus on tracking precipitation areas and/or simulated radar reflectivity rates. Since we are interested in PV anomalies associated with storm updraughts, we have to track a variable that is more directly related to the updraught. We choose to track the vertical velocity, w, in the mid-troposphere. It is justifiable to use w, instead of PV, because all PV dipoles will have a diabatic origin and will therefore be associated with a w anomaly. Although PV might seem to be the most logical and worthwhile variable to track, since it is the variable directly tied to the coherent structure of the storm, there are several advantages to tracking w instead of PV:

- Tracking using w is cleaner in the sense that less splitting and merging occurs for w anomalies than PV anomalies.
- PV is a consequence of the diabatic anomalies associated with convection. Therefore the w anomaly intensifies first, before the PV anomalies appear. Hence, it is easier to follow the intensification process of the PV dipole.
- During the intensification period of w, the PV dipole will be centred across the updraught. Therefore, it is easier to identify a PV dipole associated with a convective cell using tracks of w.

A disadvantage of tracking w is that one cannot follow the PV dipoles after the updraught has vanished. Since the PV dipoles are tilted in the vertical, they might survive for a significant time after the original updraught has died out (Chagnon and Gray, 2009). Therefore it could also be useful to track PV for cases where is is possible (i.e. for those where splitting and merging of the PV anomalies do not occur).

2.5. Tracking methodology

To reduce noise in the w field, the w at level 23 ($\approx$ 5.8 km) is Gaussian filtered, i.e. we compute the convolution of w with the Gaussian $g(x, y)$,

$$g(x,y) = \frac{1}{2\sigma^2} \exp\left(-\frac{x^2+y^2}{2\sigma^2}\right), \quad (1)$$

where x and y denote the distance from the origin (i.e. the point at which the Gaussian filter is applied) in the longitudinal and meridional direction, respectively. We choose a standard deviation σ of one grid point, and we calculate the Gaussian convolution only in a 5×5 grid point environment. In this environment $g(x, y)$ is normalized, so that the sum of $g(x, y)$ is equal to 1.

The reason we select a level in the middle troposphere is that we only want to select the deep convective cells. As shown in Weijenborg *et al.* (2015), 5.5–6 km is about the height where we expect maximum PV anomalies. We determine maxima of w every 2.5 min, i.e. we calculate local maxima of the Gaussian-filtered w exceeding 1 m s^{-1} for every output time (Figure 3). For each of these maxima, its next location is predicted using an environmental wind. It is assumed that the storm moves with this environmental wind, which is calculated in a 19×19 grid point environment of the updraught. If there is a maximum w in the neighbourhood of the predicted maximum (i.e. within $\pm$ 2 grid points of the predicted maximum (Figure 3), the two maxima are connected. If there are multiple maxima in the vicinity of the updraught, the track is tagged as problematic and results are not used. During the tracking, the variables (PV, u etc.) are saved in a 31×31 grid point (86.8 $\times$ 86.8 km) environment of the maximum Gaussian-filtered w. Only tracks that last at least 30 min are saved.

The time interval we use in tracking, 2.5 min, is about the minimum that shows changes between times (six times the time step of the model). The tracking method is relatively simple; an advantage of this is that determining composites is easy compared to more advanced object-based tracking algorithms. The temporal resolution should be high enough to capture all changes. Assuming a horizontal speed of the updraught of 30 m s^{-1}, the maximum movement expected of an updraught in 2.5 min is 4.5 km (1.5 grid points).* Figure 3 shows that 2.5 min is a reasonable choice. There is considerable evolution between the 0 and 10 min times. There are four maxima at the 0 min time, but only two at the 10 min time. It would be difficult to connect the maxima with each other between these two times. One could argue that tracking is still possible with a 5 min time interval, but we choose 2.5 min to improve the accuracy of the tracking.

2.6. Rotation of convective cells

Since the dipole of PV will be orientated along the large-scale wind shear (Figure 1), the height-integrated PV dipoles will be orientated in different directions for the different cases. Therefore, the fields of the individual cells have to be rotated to ensure that the orientation of the PV dipole is consistent. Every storm is rotated in such a way that the bulk wind shear is in the eastern direction. The large-scale wind shear is calculated as the horizontal mean wind velocity difference between 0 and 6 km in a 19×19 grid point (53.2 $\times$ 53.2 km) environment of the Gaussian-filtered velocity maximum. The variation in orientation of bulk wind shear (Figure 4) shows that rotation is necessary. Before rotation, most of the convective cells have southwesterly wind shear: exceptions are the 5 June 2011, 6 June 2011 and 30 June 2012 weather cases. For these cases the wind shear is more southerly to southeasterly (dark blue, dark red and orange symbols in Figure 4). Moreover, for 28 June 2011, for a few convective cells the bulk wind shear was from the north. In conclusion, the variation of the environmental wind shear shows that rotation is necessary.

*The maximum storm speed (averaged over the storm lifetime) over all nine cases is 32 m s^{-1}.

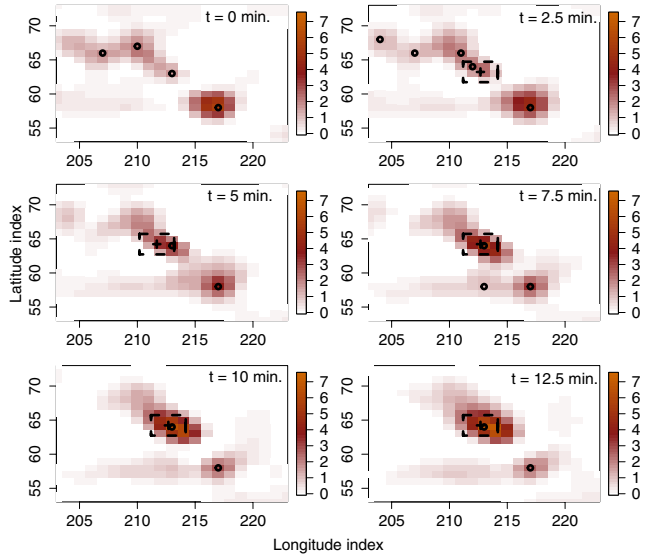

Figure 3. Schematic of the tracking algorithm. The Gaussian-filtered w is plotted (coloured contours, m s^{-1}) at times (a) 0, (b) 2.5 min, (c) 5 min, (d) 7.5 min, (e) 10.0 min, and (f) 12.5 min. The maxima of the Gaussian-filtered w are determined (○ in plots) every 2.5 min. For each maximum, the next location is predicted (+, shown for only one maximum here; text gives details). If there is a new maximum at the next time within a box of ± 2 grid points (−) from the predicted location (+), the respective maxima are connected in a track. [Colour figure can be viewed at wileyonlinelibrary.com].

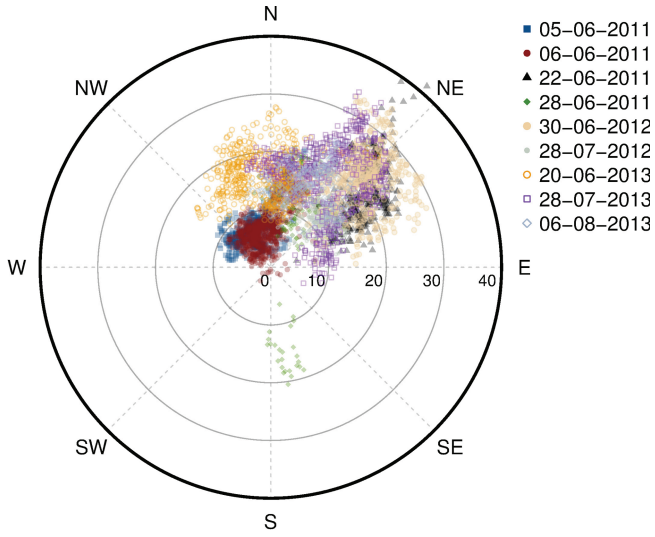

Figure 4. Average bulk wind shear, in a 19 × 19 grid point environment around the Gaussian-filtered w. Each point indicates the direction of the bulk wind shear (0–6 km wind velocity difference), and the nine different weather cases are indicated by different colours. The values on the x-axis indicate the bulk wind shear in m s^{-1}; a circle is drawn for every 10 m s^{-1}. [Colour figure can be viewed at wileyonlinelibrary.com].

2.7. *Compositing*

We want to derive a composite that characterizes a typical convective cell. However, the duration of the different cells differs considerably. Therefore, we first centre the composites around the time of the maximum Gaussian-filtered w. This will be defined as the 'reference time'. Second, we exclude cells that have more than one w maximum during their evolution. Although this is a considerable fraction of the cells (about one third), we want to make sure that before the reference time the cell intensifies and that the decay phase starts after the reference time. All composites of PV in section 4 are height-integrated composites from 3 to 7.3 km height, as in Weijenborg *et al.* (2015). For the PV and horizontal wind velocity, anomalies are calculated by subtracting the spatial mean (in a 31 × 31 grid point environment) over the whole lifetime of the cell.

Table 2. Convective cell environment variables.

Variable	Definition and remarks
Instability parameters	
CAPE	Convective available potential energy, CAPE and other instability parameters are calculated for an air parcel with thermodynamic properties of the lowest 50 hPa of the PBL.
CIN	Convective inhibition.
Shear parameters	
$SRH_{0-1\,km}$	Storm relative helicity, integrated from 0 to 1 km height. Storm motion is estimated from the average motion over the whole lifetime.
$SRH_{0-3\,km}$	SRH, integrated from 0 to 3 km height. Storm motion is estimated from the average motion over the whole lifetime.
Bulk wind shear	The magnitude of the wind velocity difference between 6 and 0 km height. Wind velocities at model level 23 (≈ 5.8 km) and at 2 m are used.
Moisture parameter	
HDIV	Vertically-integrated divergence of specific humidity q_v.

All variables are calculated from the mean value in a 31 × 31 grid point environment around the storm updraught, 15 to 0 min before the time of the maximum Gaussian-filtered w.

Table 3. Convective cell property variables.

Variable	Definition
Max. intensity	Maximum Gaussian-filtered w (m s^{-1}), during the lifetime of a cell.
w maximum	Maximum w (m s^{-1}), during the lifetime of a cell.
PV maximum	Maximum PV anomaly (PVU, 1 PVU ≡ 1 × 10^{-6} km^2 s^{-1} kg^{-1}) in a 5 × 5 grid point environment of the updraught, during its whole lifetime.
Correlation r	Correlation coefficient r. This measures how well the maximum PV anomaly and the updraught are correlated (Weijenborg *et al.*, 2015).
Precipitation rate	Precipitation rates (mm h^{-1}), averaged over a 11 × 11 grid point environment of the updraught.

For every cell, environmental characteristics including CAPE, CIN, SRH and bulk wind shear are calculated (Table 2). For SRH, we use for every convective cell its average storm speed c during its lifetime. The goal is to calculate the environmental characteristics for each cell; however, the buoyancy and instability indices particularly are strongly influenced by the updraught itself. For example, convection stabilizes the atmosphere and therefore CAPE will be reduced during convection. To avoid this influence of the cell, we calculate the storm environmental properties in a 31 × 31 grid point environment 30 to 15 min before the tracking starts. The exact time differs for each convective cell because the data for environmental parameters such as CAPE is only available at 15 min temporal intervals (section 2.3).

In addition to the storm environment properties, we calculate characteristics of convective cells including maximum and minimum PV and their starting location of tracking (Table 3). Moreover, we want to investigate how the PV anomalies differ for 'extreme' cells. Therefore the model precipitation rates are determined in a 15 min time frame around the maximum Gaussian-filtered w.

Weijenborg *et al.* (2015) used a correlation coefficient r, based on Davies-Jones (1984), as a measure of how much the updraught and the positive PV pole are correlated. As in Weijenborg *et al.* (2015), r in Table 3 is defined as

$$r = \frac{< \mathrm{PV}w >}{(< \mathrm{PV}^2 >< w^2 >)^{1/2}}. \qquad (2)$$

The angular brackets denote a height-weighted mean integral (from 3 to 7.5 km, in a 3×3 grid point region surrounding the updraught).

As for the composites in Weijenborg *et al.* (2015), only the results that are significant against the null hypothesis that the anomalies are zero are plotted. Both a Student's t-test and a recurrence analysis after von Storch and Zwiers (1988) are used. Only the PV and wind velocity anomalies for which the Student's t-test can be rejected at the 0.01 significance level are presented in the plots. For the recurrence analysis, the maximum p-recurrence at which the null hypothesis can be rejected at the 0.05 significance level is calculated. A Student's t-test measures only significant differences in the mean, but this test does not tell us how large this difference is. The p-recurrence is a measure of how large the difference in means is: 69% (84%) p-recurrent implies that the experiment ensemble and a control ensemble are separated by 1.0 (2.0) standard deviations (for more details, see von Storch (1988)). In our case we test how much the PV anomalies are separated from a hypothetical control ensemble, centred around 0, with the same variance as the PV distribution. The Student's t-test and p-recurrence are both calculated at every grid point of a composite, with the sample being all the cells contributing to the composite at that location and time.

3. Variability of environmental parameters and convective cell properties

The variation of the different environmental characteristics of the cells for the nine weather cases is shown in Figure 5. Median values of CAPE for each weather case (Figure 5(a)) vary from a few hundred J kg^{-1} to about 650 J kg^{-1} for the 5 June 2011 case. These values might seem low, e.g. CAPE values associated with severe convective weather typically range from 1000 to 2000 J kg^{-1} (Thompson *et al.*, 2003). Remember, however, that the convective parameters are calculated over a large environment, 31×31 grid points around the maximum Gaussian-filtered w. Moreover, there is often convection already generated in this environment and this consumes CAPE. Furthermore, Groenemeijer and van Delden (2007) found median CAPE values of about 300 J kg^{-1} during thunderstorms in the Netherlands. The spread of CAPE is quite large: some convective cells have almost no CAPE, while other cells have CAPE above 2000 J kg^{-1}. Typically, CAPE values above 1000 J kg^{-1} occur about once or twice in southern Germany for the summer months, and CAPE values above 2000 J kg^{-1} are seldom observed in this region (Romero *et al.*, 2007). For Switzerland and Austria the occurrence is a little higher. Therefore, these values are realistic for Western Europe. CIN values (Figure 5(b)) are generally low: median CIN is less than 100 J kg^{-1} for most cases. Exceptions are the 28 June 2011 and 30 June 2012 cases, where median CIN values of 150 and 200 J kg^{-1} are observed. For the latter case (30 June 2012), 25% of cells have CIN values of more than 300 J kg^{-1}.

The shear-related variables show a similar variation between the nine cases. The median of SRH (Figure 5(c)) varies between almost zero for the 5 and 6 June 2011 cases, up to 100 m^2 s^{-2} for two of the three cases in 2013. Considering supercells, Thompson *et al.* (2003) found that the mean 0–3 km height-integrated SRH is about 180 m^2 s^{-2} for non-tornadic supercells and about 250 m^2 s^{-2} for tornadic supercells. Similarly high values (> 200 m^2 s^{-2}) are found in all the cases, but most often in the 30 June 2012 and 28 July 2013 cases. The bulk wind shear (Figure 5(d)) also shows sufficient spread. For a few cases (5 and 6 June 2011), the wind shear is weak with median values of about 8 m s^{-1}. There are about five cases with moderate vertical wind shear (10–20 m s^{-1}). Strong shear cases are 22 June 2011 and 30 June 2012 in which the median bulk wind shear is larger than 20 m s^{-1}; such high values of the wind shear can be an indicator for supercells (e.g. Thompson *et al.*, 2003). As for the other parameters, the spread in the bulk wind shear is large: it has extremes up to 40 m s^{-1}.

Other convective variables, such as the Showalter Index (SI) and Lifted Index (LI), show similar spread for the different cases (not shown). In conclusion, there is sufficient variation in the synoptic-scale and mesoscale background of the cells to create representative composites.

The spatial distribution of the tracked convective cells (Figure 6) shows that convective cells are found mainly within a band from northeastern France to northeastern Germany. A further (small) maximum can be found in northwestern Germany, at the border with the Netherlands. Moreover, there are a lot of cells in Switzerland which probably are generated orographically. The relatively low average values of CAPE in this region (not shown) are consistent with this hypothesis.

4. Composites

4.1. Diabatic forcing

Before we look at the composites of PV and corresponding flow anomalies, we first look at composites of the vertical profile of the diabatic heating, $\dot{\theta}$. PV tendencies are contributed by a horizontal gradient in the presence of a horizontally oriented background vorticity vector (Chagnon and Gray, 2009). This PV is subsequently realized as vertical vorticity after tilting of the background vorticity by the storm updraught. For the $\dot{\theta}$ composites, we average over a 5×5 grid point region around the updraught.

Values of $\dot{\theta}$ (Figure 7(a)) maximize in the middle troposphere at the height where the Gaussian-filtered w maximizes at the reference time. This is at about 5.5 km height (Weijenborg *et al.*, 2015, and Supplementary Figure S1), with average maximum $\dot{\theta}$ values of about 0.55 K min^{-1}. The height of maximum $\dot{\theta}$ changes from about 5 km height at 15 min before the reference time (hereafter referred to as the -15 time and similarly for other times), to about 5.5–6 km height 15–30 min afterwards.

A similar pattern is seen when selecting the 10% most intense cells or the 10% weakest cells in w (Figure 7(b)). The main difference is that the $\dot{\theta}$ values are much larger, up to 1.5 K min^{-1} for the 10% of cells with largest w. This maximum is also located slightly higher up in the troposphere (at about 6.25 km). Little temporal evolution occurs for the 10% weakest w cells. For all times the $\dot{\theta}$ maximum is about 0.2–0.25 K min^{-1}.

CAPE is an indicator of instability and it is moderately correlated with w, therefore one might expect similar large differences in vertical $\dot{\theta}$ profiles between the strongest and weakest CAPE cells. However, little difference exists (Figure 7(c)). Diabatic heating is related to the temporal change of CAPE (Emanuel, 1994, p. 483) and so one cannot expect a correlation because the temporal change of a state variable and the variable itself are orthogonal properties of the flow. Moreover, theoretical understanding of the quasi-equilibrium of deep moist convection shows that the vertical convective mass flux ($\propto w$) is, to first order, proportional to the temporal change of CAPE (Emanuel, 1994, p. 514), which is directly dependent on the diabatic heating. This explains the contrasting separations in Figures 7(b) and (c). However, there are clear differences in the height of the $\dot{\theta}$ maxima. This maximum is higher in the troposphere for the intense CAPE cells (6.5 km) compared with weak CAPE cells (5.0 km). This is an indicator of deeper updraughts for these strong CAPE cells.

For intense PV (Figure 7(d)) and intense precipitation cells (Figure 7(e)), the maximum $\dot{\theta}$ is slightly smaller than for the strong w cells, reaching about 1.2 K min^{-1} at the time of maximum Gaussian-filtered w. However, the general structure and the temporal evolution are very similar to those of the intense w cells. This can be explained by the notion that the PV anomalies are caused by the diabatic heating, which is proportional to the updraught strength. Similarly, Figure 7(e) can be explained

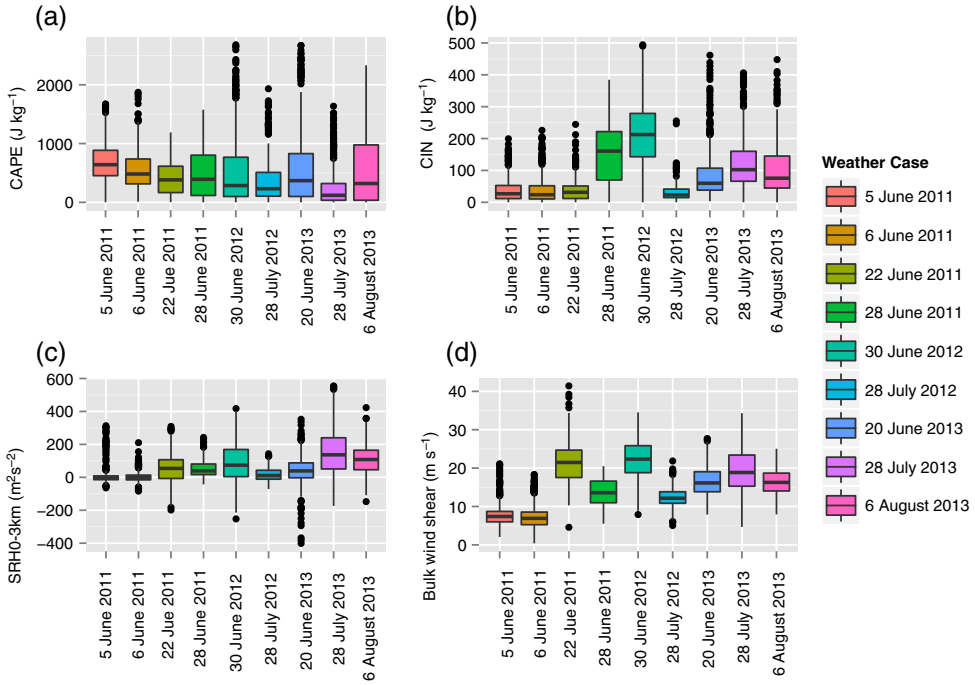

Figure 5. Environmental characteristics for the convective cells in the nine different weather cases. (a) CAPE, J kg^{-1}, (b) CIN, J kg^{-1}, (c) SRH, integrated over 0–3 km height, m^2 s^{-2}, and (d) bulk wind shear, m s^{-1}. The colours indicate the different weather cases, and the box plot indicates the variation of the respective variable for that weather case. In each box plot, the upper and lower hinges indicate the first and third quartiles. The upper and lower whiskers extend up to 1.5 times the interquartile range (i.e. the difference between the first and third quartiles). Outliers beyond the whiskers are indicated by points. [Colour figure can be viewed at wileyonlinelibrary.com].

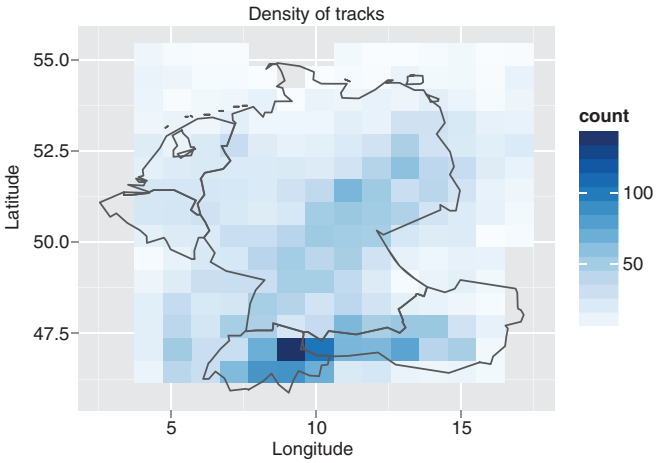

Figure 6. The number of tracked convective cells initiated in each box of ~ 65 × 65 km. [Colour figure can be viewed at wileyonlinelibrary.com].

by the precipitation rate being related to the moisture flux and therefore the updraught strength. In conclusion, maximum diabatic anomalies (and therefore PV anomalies) are found at approximately 5.5 km height. The next section will discuss the height-integrated PV composites.

4.2. *General evolution*

Figure 8 shows the composite over all 3135 tracked cells from the nine selected cases. It is remarkable that, even with this large number of cells, a clear PV dipole is visible, orientated as expected from Figure 1 along the west–east axis (remember that we rotated the cells in such way that the wind shear is eastwards). The orientation is exactly as hypothesized in Weijenborg *et al.* (2015), with a positive PV anomaly in the south and a negative PV anomaly in the north. The updraught is almost perfectly in the centre between the positive and negative PV poles until the reference time of the maximum Gaussian-filtered w (Figures 8(a) and (b)). At the −30 min time (Figure 8(a)), the correlation coefficient r is about 0.25. Slightly later, at the −15 time, the updraught is still approximately centred (not shown). No large changes are found up to the reference time (Figure 8(b)). The horizontal wind speed anomalies of 2.45, 2.31 and 3.73 m s^{-1} at the −30, −15 and reference times, respectively, are relatively small compared to the average environmental wind of about 13–14 m s^{-1}. This maximum horizontal wind velocity anomaly is located at the updraught between the positive and negative PV poles. Although the cyclonic flow around the positive PV pole is clearly visible, the anticyclonic flow around the negative PV pole is less clear. An explanation could be that the positive anomaly is generally significantly stronger than the negative anomaly.

Of the 3135 cells at the reference time (Figure 8(b)), 2605 (83.1%) cases survive for at least 15 min, but only 1124 (35.9%) cells survive for 30 min (Figure 8(c)) and 353 (11.26%) cells for 45 min (Figure 8(d)). Note that the intensification phase of the cell is much shorter than the decay phase. Whereas at the −30 time only 580 cells contribute to the composite, about double that number (1124) contribute to the composite at the +30 time.

The magnitude of the PV maximum stays approximately constant: the maximum PV decreases from 4.85 PVU at the reference time to 4.21 PVU at the +45 time. Weijenborg *et al.* (2015) found that especially intense convective cells show a more monopole structure, in which the positive PV pole is dominant compared to the negative pole. We also see this in the composite for the longer-lasting convective cells. The positive PV anomaly is moved slightly northwards in Figures 8(c) and (d). As for the composites for the 22 June 2011 case, the positive PV pole clearly dominates, especially after the reference time: at the +30 time (Figure 8(c)) the magnitude of the positive PV pole (4.03 PVU) is almost twice as large as that of the negative PV pole (2.18 PVU). This asymmetry is even stronger at the +45 time (Figure 8(d)). For the +30 and +45 times there are only significant cyclonic flow anomalies, which are associated with the positive PV pole. Vertical cross-sections from south to north show a similar picture (Figure S1). Although the strength of the dipole decreases, the depth of the dipoles is reasonably well maintained.

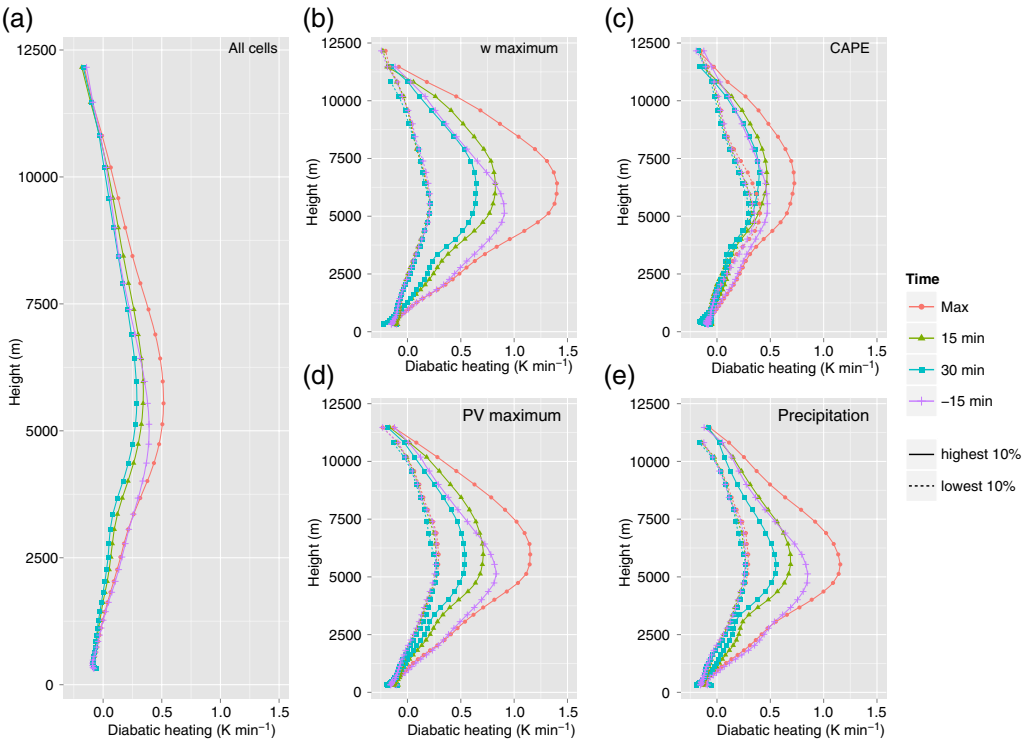

Figure 7. Composites of the vertical diabatic heating (K min^{-1}) profile for four different times relative to the time of the maximum w (the times are of the maximum, 15 and 30 min after and 15 min before this time), (a) is for all cells, and (b–e) are for the convective cells with the lowest 10% (dotted) and highest 10% (solid) (b) Gaussian-filtered w, (c) CAPE, (d) PV maximum and (e) precipitation rates. [Colour figure can be viewed at wileyonlinelibrary.com].

The question addressed in this study is whether significant and consistent PV anomalies exist. We have shown that there are significant PV anomalies during the whole convective lifetime. Average anomalies are on average one order of magnitude larger than mean synoptic-scale and planetary-scale values (in the middle troposphere), which are about 0.5 PVU. The goal was to analyse whether there are statistically coherent dipoles, with associated flow anomalies. The composites in Figure 8 show that, even when averaging over many convective cells in different environments, we get a clear PV dipole with associated cyclonic flow anomalies. The anticyclonic flow anomalies are less clear, although they become clearer when we make a composite excluding the 10% strongest PV cells (not shown). The variability in the PV anomalies is quite large as quantified by the recurrence analysis: p-recurrence values of the PV maxima (minima) are 63.5% (59%) p-recurrent at the reference time.

4.3. *Evolution of extreme cells*

For the 5 and 22 June cases, the particularly intense cells showed a 'supercell structure' (Weijenborg *et al.*, 2015). The diabatic heating rates for intense w cells, intense PV cells and cells with strong precipitation rates are very similar (Figure 7). Moreover, these different kind of intensity measures are highly correlated. One would therefore expect also similar PV composites. This is indeed the case as shown in Figure 9.

For all three intensity measures, the positive PV pole is correlated with the updraught, even at the reference time. For the 10% strongest w cells (i.e. the cells with a w exceeding 7.71 m s^{-1}; Figure 9(a)), the PV maximum (11.6 PVU) is clearly stronger than the PV minimum (−5 PVU). Because the 10% strongest cells are selected, the number of cells is reduced and there are 314 cells included in these composites. Half an hour later (Figure 9(b)), the positive PV anomaly is only slightly weaker (9.1 PVU), while the negative PV anomaly is almost half (−2.7 PVU) the earlier value. About 139 (approximately 44%) convective cells survive for 30 min; this survival rate is larger than that for all cells (which is about 35%; Figure 4.2).

Strong PV cells (Figures 9(c) and (d)) show a similar morphology to strong w cells. Maximum PV values are of course larger for the intense PV composite, with a maximum of more than 14 PVU at the reference time (Figure 9(c)). The number of cells at the +30 time is also larger than with the intense w cells; about 149 (47.5%) of the convective cells survive until the +30 time. As for the intense w cells, there is a strong asymmetry in the PV dipole; the positive PV anomaly is almost four times as strong as the negative PV anomaly at the +30 time (Figure 9(d)). Moreover, the maximum horizontal wind velocity anomaly also increases: it is about 7.7 m s^{-1} in Figure 9(c) and 5.5 m s^{-1} in Figure 9(d). Consistent with the strong asymmetry in the PV dipole, only a clear cyclonic flow around the positive PV anomaly is observed.

Heavy precipitation cells (Figures 9(e) and (f)) also are strongly asymmetric. The corresponding PV anomalies are weaker than those in the strong w and PV cells. However, the PV anomalies are still two to three times stronger than those in the composites over all cells. In conclusion, we see that the morphology of intense cells shows a clear dominant 'supercell' structure: an intense long-lasting rotating updraught. Although this is a trivial result for the intense PV composite, since we selected the 10% cells with the largest PV maxima, it indicates again that the different intensity measures are correlated even in their extreme ranges. Cross-sections of PV and w show a similar picture for strong PV and strong precipitation cells, with a more monopole morphology, especially at the +45 time (see also Figures S1–S3).

Selecting higher thresholds for making the composites, namely the top 5 and 2.5% of cells in PV and precipitation, gives even stronger PV composites and a clearer monopole structure (shown at the +30 time in Figure 10). Even though this is 30 min after the time of the strongest updraught, the intense PV convective cells have an average maximum PV anomaly of 12 PVU for the 5% most intense cells (Figure 10(a)) and almost 14 PVU for the 2.5% most intense cells (Figure 10(b)). Although there is still a small negative PV anomaly visible in the composite of Figure 10(a), there is only cyclonic flow. Flow anomalies are also larger, with maxima of over 7 m s^{-1}, even after 30 min. At the reference time

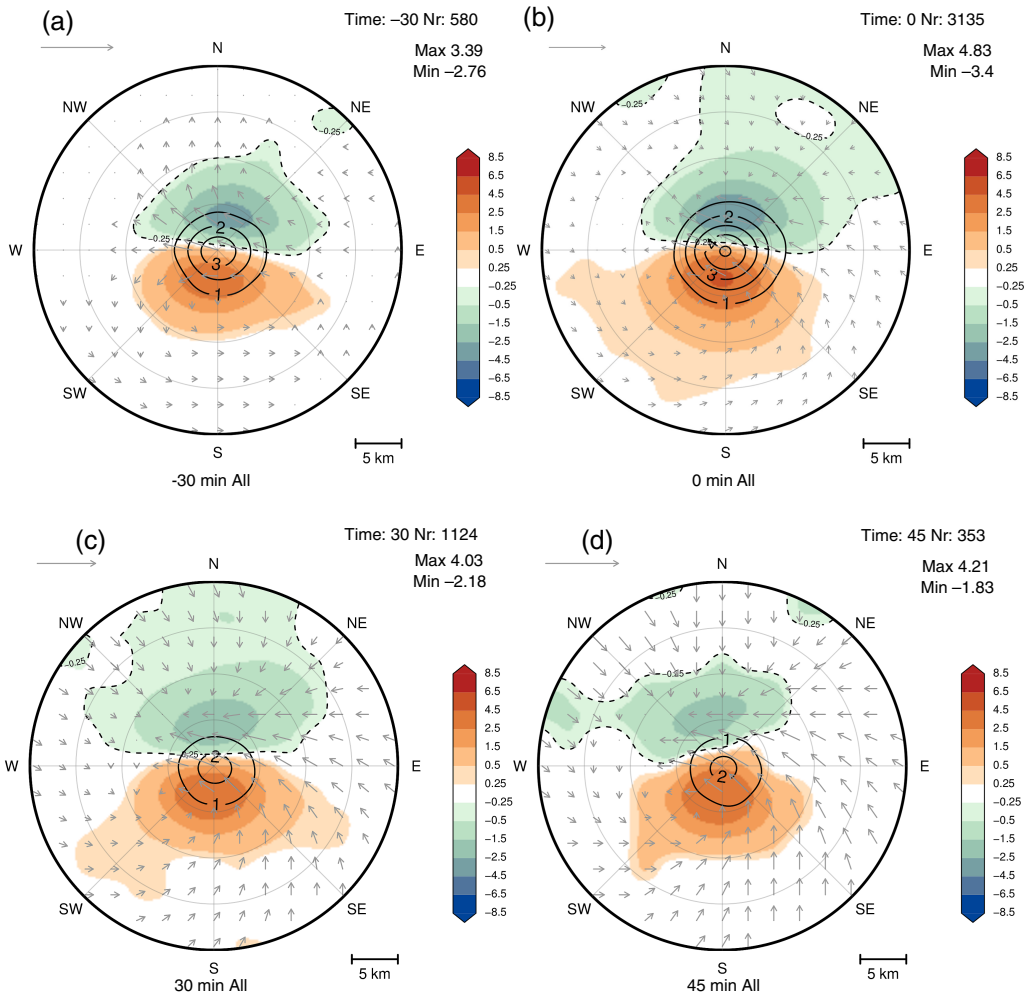

Figure 8. General evolution of cells at (a) −30 min, (b) 0 min, (c) +30 min, and (d) +45 min relative to the time of the maximum (Gaussian-filtered) w (denoted as the reference time). Filled contours denote PV anomalies (in PVU), contour lines indicate w (non-filtered, m s^{-1}) and arrows denote horizontal wind velocity anomalies. The negative PV anomaly is indicated by the dashed contour line. All fields are height integrated between 3 and 7.3 km height. A reference vector of 5 m s^{-1} is added at the top left. At the top right of each panel are indicated the time (in minutes relative to the time of the maximum Gaussian-filtered w), the number of cells in the composite, and the spatial maximum and minimum PV of the composite. Only the significant anomalies are plotted; text gives more details. [Colour figure can be viewed at wileyonlinelibrary.com].

(not shown), the PV maximum is even stronger (almost 20 PVU for the 2.5% strongest PV cells, with flow anomalies of more than 9 m s^{-1}). However, the monopole morphology is less clear.

The composites of convective cells with large precipitation rates (Figures 10(c) and (d)) are again very similar to the strong PV cells, although maximum PV anomalies are slightly weaker; 8.6 PVU and 10.0 PVU for the composites with the 5 and 2.5% strongest cells respectively. For these severe precipitation cells, there is a significant w anomaly about 20 km downshear, indicating the generation of a new updraught downshear of the existing updraught.

4.4. *Influence of environment on cell morphology*

The morphology of cells can strongly depend on the convective environment. For example, Thompson *et al.* (2003, 2007) found that strong shear and/or strong SRH is a good predictor for supercell-like cells. Moreover, the wind shear might also influence the morphology of the PV anomaly, by advecting the dipoles downshear. We therefore look at the composite for the convective cells with the 10% largest values for the buoyancy parameters CAPE and CIN and the shear parameters bulk wind shear and SRH (integrated over both the lowest 1 km and the lowest 3 km of the atmosphere). For the moisture variable, the vertically-integrated divergence of specific humidity (HDIV), the composites are made for the 10% lowest values because, for deep moist convection, convergence is more relevant as indicator for convection than divergence. For these composites, only the +30 time is plotted in Figure 11.

Although there is a moderate correlation between w and CAPE (correlation coefficient of about 0.49, not shown), the composite for strong CAPE cells (Figure 11(a)) does not resemble that of the strong (Gaussian-filtered) w cells. The w is related to the vertical convective mass flux, which is related to the temporal change of CAPE. PV anomalies are weaker compared to the intense w composite and, although the positive PV pole is stronger than the negative PV pole (respectively 6.8 and −3.4 PVU), the updraught is almost centred between the dipole. The updraught is of similar strength at the +30 time to that in the intense PV and intense precipitation composites, at about 5 m s^{-1}. For the composite using the convective cells with strong CIN (Figure 11(b)), the asymmetry is clearer, although the PV anomalies are weaker. In the COSMO model, the CIN is defined as the negative buoyancy up to the level of free convection (LFC). These large values indicate that the planetary boundary layer is very stable; significant lifting is necessary to initiate convection.

The composites of strong SRH cells (Figures 11(c) and (d)) show a dominant positive PV anomaly, but not as clearly as for the intense PV and precipitation cells. The 0–1 and 0–3 km integrated SRH composites have very similar morphologies, with the main difference being that for the former there is still a significant negative PV anomaly. The PV maximum is not much stronger than for the general composite in Figure 8 (4.8 and 5.4 PVU for the 0–1 km and 0–3 km SRH composites, respectively). For both

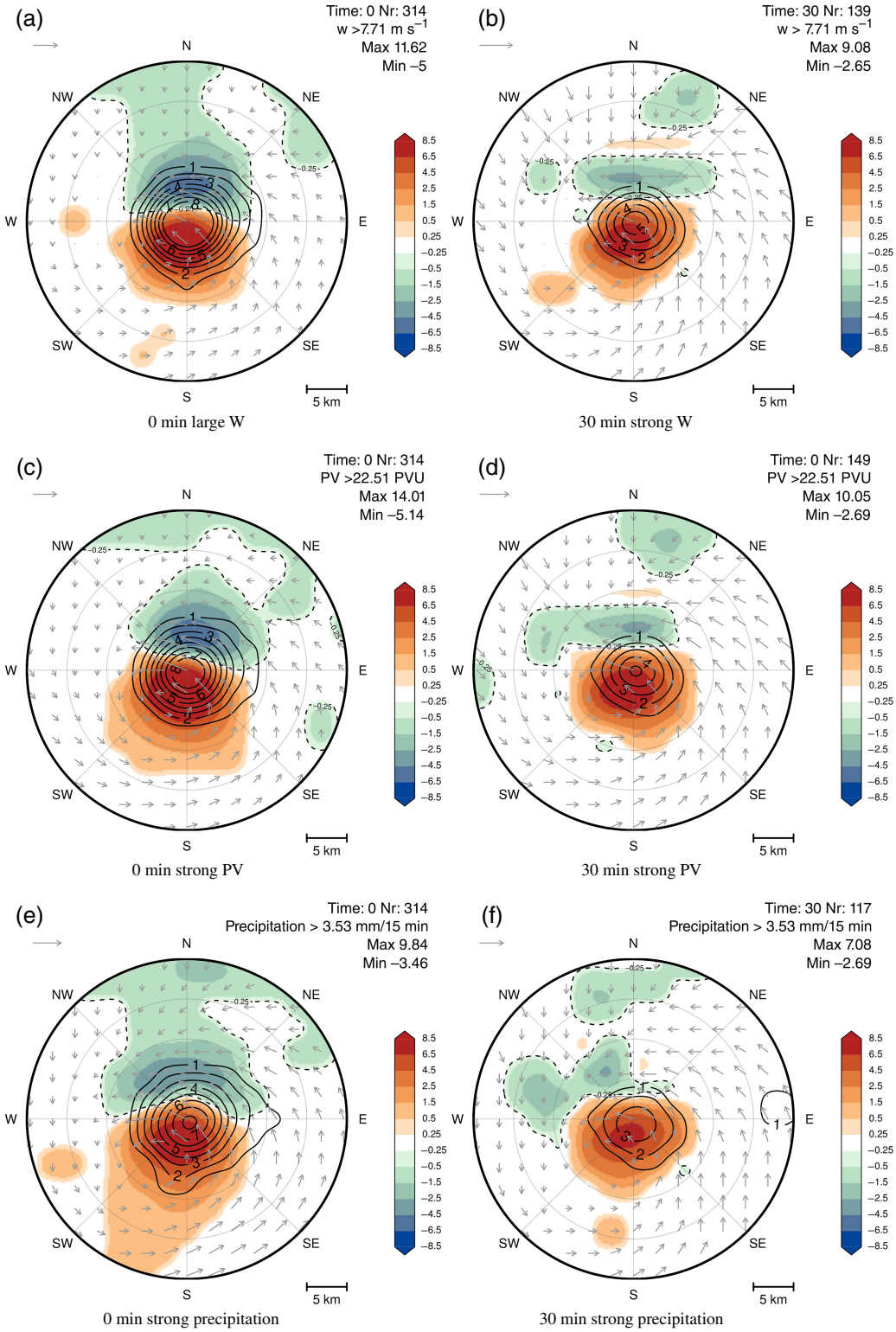

Figure 9. Evolution of the cells for the cells with the 10% largest values of (a, b) Gaussian-filtered w, (c, d) PV, and (e, f) precipitation, for different times. Here the reference time is the time with maximum (Gaussian-filtered) w. Filled contours denote PV anomalies (in PVU), contour lines indicate w (non-filtered) anomalies ($m\,s^{-1}$) and arrows denote horizontal wind velocity. The negative PV anomaly is indicated by the dashed contour line. All fields are height integrated between 3 and 7.3 km height. A reference vector of $5\,m\,s^{-1}$ is added at the top left. Indicated at the top right are the time (in minutes after the maximum Gaussian-filtered w), the number of cells in the composite, the threshold of the respective variable used in the composite, and the spatial maximum and minimum PV of the composite. Table 3 gives definitions of how the maximum PV and precipitation rates are calculated. Note that in (a) and (c) not all w contours are plotted; the respective maxima are 11.33 and $9.52\,m\,s^{-1}$. [Colour figure can be viewed at wileyonlinelibrary.com].

composites, the PV dipole is slightly rotated in the clockwise direction. We rotated every convective cell with the bulk wind shear difference between 0 and 6 km. Strong (positive) SRH indicates a clockwise hodograph, which explains the different orientation of the dipole.

For the convective cells with strong bulk wind shear (Figure 11(e)), the PV dipole is more stretched out than the other composites we have seen so far. Weijenborg *et al.* (2015) found that, for the high-shear 22 June weather case, the dipoles orientate in PV bands. This is another confirmation that advection effects associated with the wind shear play a role in the formation of PV bands. The composite for the cells with the 10% lowest wind shear values are more local and the dipole is rotated counter-clockwise (not shown).

For the moisture variables such as the HDIV, there are few differences compared to the general composite in terms

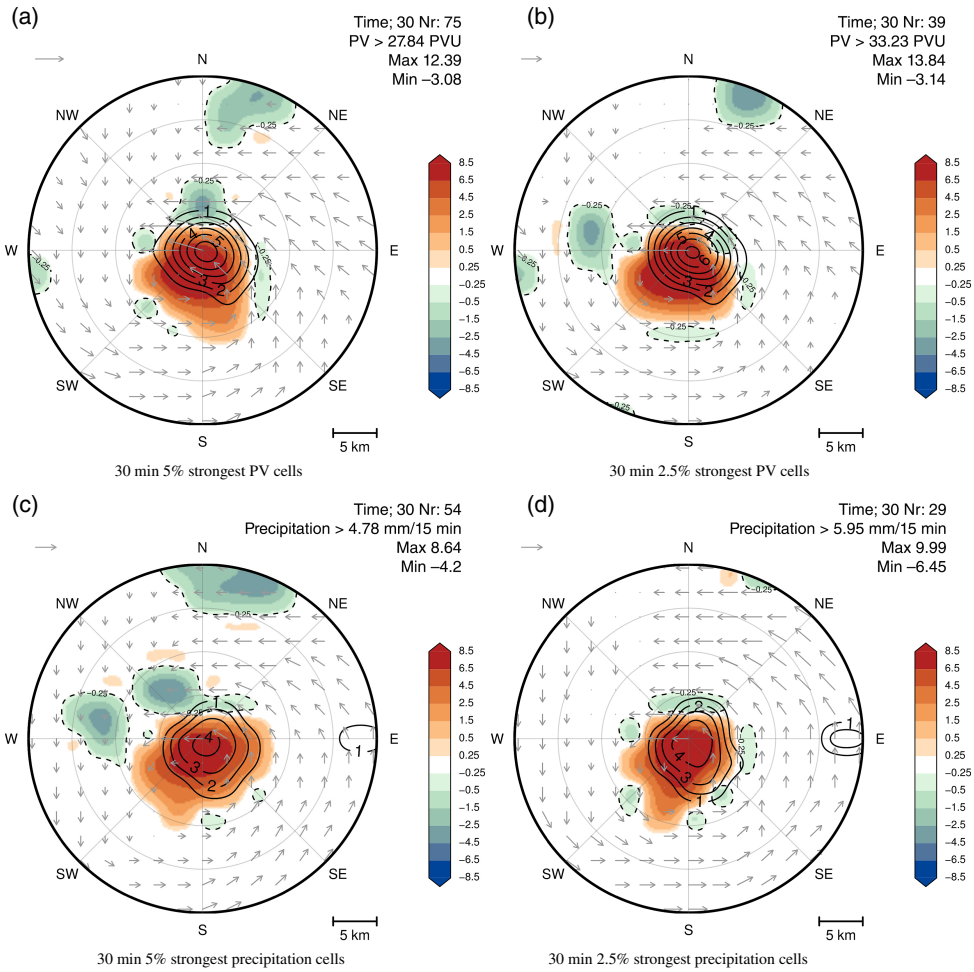

Figure 10. Composite for the cells with the 5 and 2.5% largest values of (a, b) PV and (c, d) precipitation, at the +30 time. Filled contours denote PV anomalies (in PVU), contour lines indicate (non-filtered) w anomalies ($m\,s^{-1}$) and arrows denote horizontal wind velocity. A reference vector of $5\,m\,s^{-1}$ is added at the top left. [Colour figure can be viewed at wileyonlinelibrary.com].

of magnitude of the PV anomalies. But, as for the strong SRH composites, the PV dipole is rotated clockwise. We did not find an explanation of this different orientation; HDIV is not correlated with the SRH variables, so that cannot be an explanation.

In conclusion, differences exist between convective cells in COSMO-DE initiated in different convective environments, but these differences are less clear than one might expect from the differences between strong and weak convective cells. Strong CAPE cells have stronger PV anomalies than general cells, but the PV anomalies are weaker than for intense cells. Moreover, the dipole asymmetry is also not as strong. Although there are hints of a more monopole morphology structure in the composite of strong SRH, it is not as clear as that for the intense cells discussed in section 4.3. The studies of Thompson *et al.* (2003) have already indicated that, as well as strong SRH, significant CAPE and bulk wind shear might also be needed for the formation of supercells. Moreover, they and others (e.g. Groenemeijer and van Delden, 2007) found that the variability of environments in which supercells are formed is large. Therefore a clustering using a combination of thresholds for different variables might be necessary to get the more 'monopole' morphology found for intense cells.

4.5. *Monopole characteristics of extreme cells*

We now return to the intense cells. We have seen that in the intense cell composites the maximum w and the positive PV anomaly are correlated. The median correlation coefficient, r, as a function of time since the reference time is plotted for different thresholds of the PV maximum in Figure 12(a). Except for the weakest 25% PV cells, there is a consistent increase of r for increasing thresholds. For the 10 and the 5% strongest PV cells, there is a clear increase in r just before the maximum (Gaussian-filtered) w has been reached.

A similar picture appears for the strong precipitation cells (Figure 12(b)). Especially for the cells with the 10 and 5% strongest precipitation rates, there is a very strong correlation between the w and PV. For convective cells with the 5% strongest precipitation rates, r increases up to 0.75 after the reference time. This confirms the conclusion, drawn in section 4.3, that particularly intense cells have a more monopole structure. However, one has to note that convective cells with weak precipitation rates (the weakest 25%) also have a high r value. For these cells one has to be careful in interpreting r, since the w and PV anomalies are generally small in magnitude.

In Figure 12(c), r is plotted as a function of time for different SRH thresholds. There is a consistent increase of r for increasing thresholds of the SRH. A difference is that the increase in r over time is not as sudden as for the strong PV and strong precipitation cells in Figures 12(a) and (b). This confirms the findings in the previous section that the SRH cannot completely explain the monopole structure of the intense cells.

5. Conclusion and discussion

The structure and magnitude of the PV anomalies on the convective-weather scale give valuable information which is currently not yet exploited. In this study we hypothesized that the PV might be coherent. We deliberately did not address the question of whether the PV dipoles are balanced. The main aim in calculating the composites was to determine the general structure and evolution of PV anomalies around cells modelled in a non-hydrostatic NWP model.

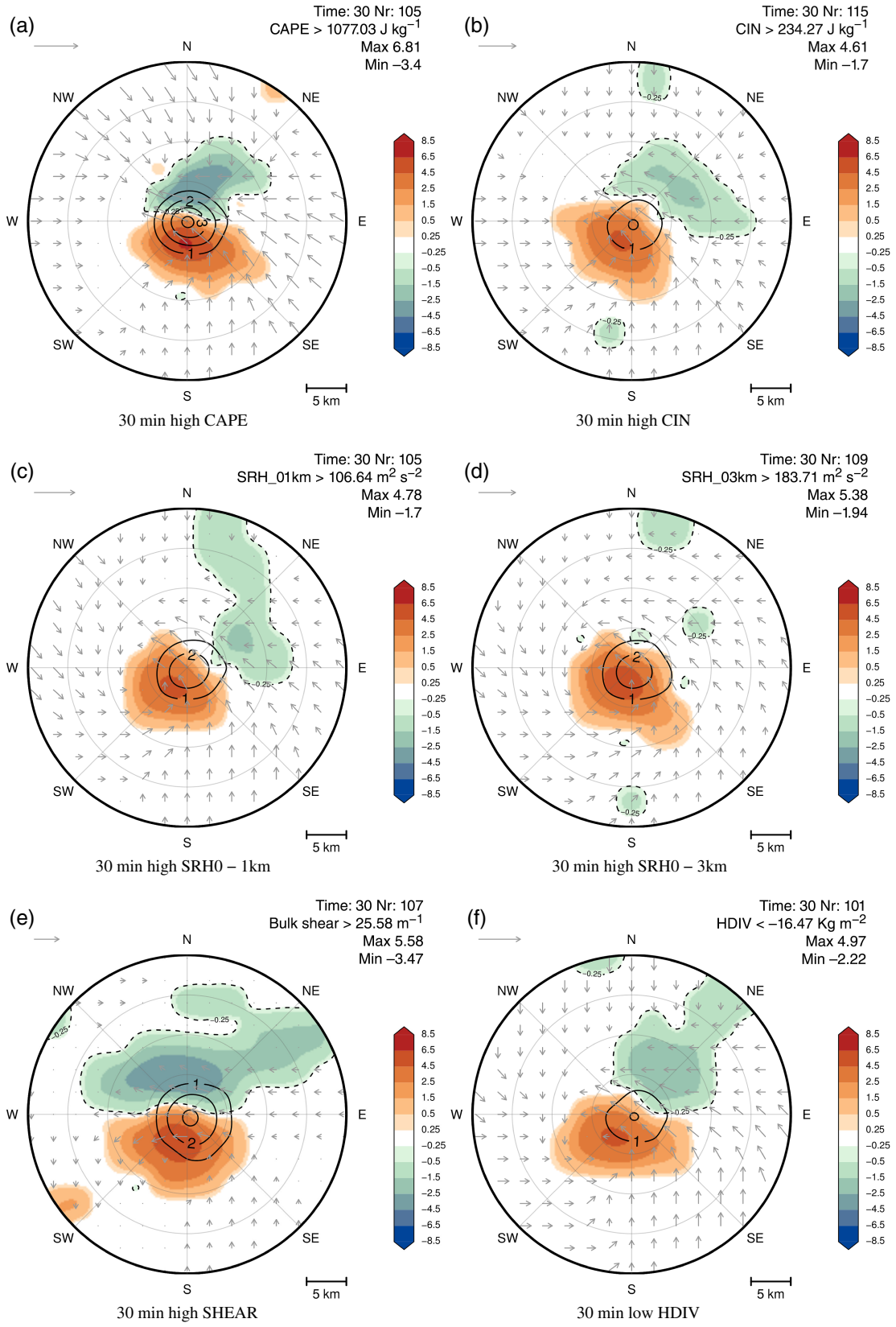

Figure 11. As Figure 10, but for cells with the 10% largest values of (a) CIN, (b) CAPE, (c) the 0–1 km SRH, (d) the 0–3 km SRH, and (e) the bulk wind shear and for cells below the 10% threshold of (f) HDIV. Table 2 indicates how the parameters are calculated. [Colour figure can be viewed at wileyonlinelibrary.com].

It is remarkable that, even when averaging over cells associated with nine highly variable cases, a coherent PV dipole (evolution) exists. The strength of the PV and associated flow anomalies consistently increase with increasing updraught strength. The most intense cells, regardless of whether one measures intensity by w, the PV anomalies or precipitation rates, show a more monopole structure which resembles supercells (a long persistent rotating updraught). This has been attributed by, for example, Thompson *et al.* (2003) to strong SRH environments. Although strong SRH cells do show a similar supercell structure, this is less clear than for strong precipitation and strong PV cells. Although there are qualitative differences, the associated flow anomalies are remarkably similar to those on synoptic and sub-synoptic scales. We did not show static stability composites; Weijenborg *et al.* (2015) found that the static stability anomalies are small inside the dipole. In summary, the results of this study confirm

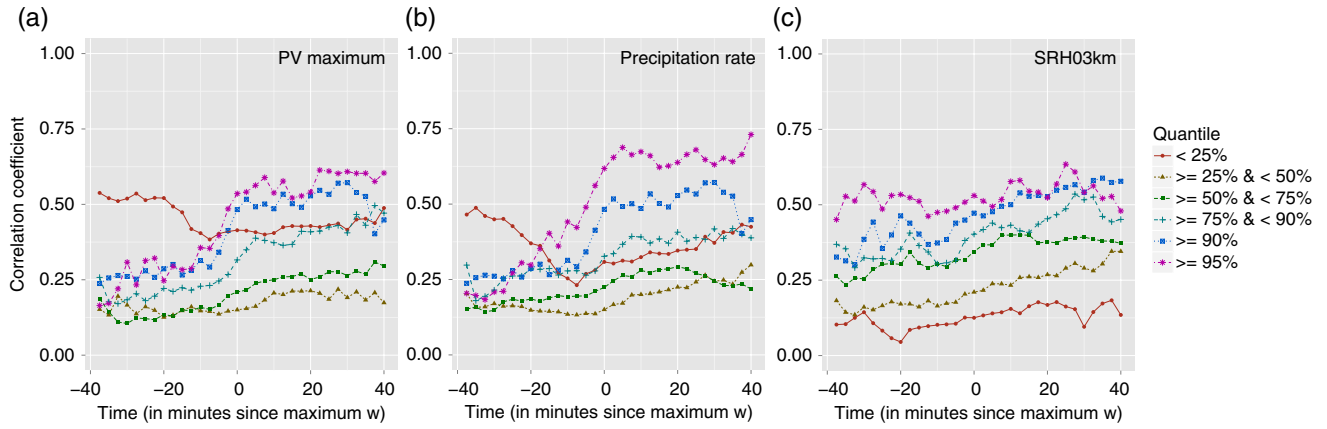

Figure 12. Median correlation coefficient, r, between w and PV, as a function of time (relative to that of the maximum Gaussian-filtered w). For exceedence of different percentiles of (a) the PV maximum (PVU, as defined in Table 3), (b) precipitation rates (mm h^{-1}) and (c) the SRH (m^2 s^{-2}, 0–3 km height-integrated). [Colour figure can be viewed at wileyonlinelibrary.com].

that there are still consistent flow anomalies associated with PV anomalies on the convective-weather scale, as for the synoptic PV anomalies described in Hoskins *et al.* (1985).

Hakim (2008) argued that the main goal in balanced dynamics is to accurately compress information into fewer variables, which they called 'control' variables. On synoptic and planetary scales, a natural choice for a control variable is the PV, since the dynamics for the QG system compress into this variable (Hakim, 2008). We have shown that PV might also be usable as a control variable on the convective-weather scale.

We did not explicitly state what kind of balance is to be expected, and how much of the flow is unbalanced. Although a PV inversion is by no means trivial, a possible pathway is using the methodology described in Viúdez and Dritschel (2004), who explicitly take the unbalanced flow into account. Another pathway could be probabilistic PV inversion Hakim (2008) and Hakim and Torn (2008). Their probabilistic theory for balanced dynamics shows similarities with an ensemble Kalman filter (Evensen, 1994), where the PV takes the role as 'perfect' observations (i.e. vanishing observation-error covariance).

Our results, and the theoretical analysis of Chagnon and Gray (2009), indicate that the PV dipoles have a longer lifetime than the convection that initiated them. The dipoles might influence the flow and/or initiate new convection even after the original updraught has died out. Weijenborg *et al.* (2015) found that in strong-shear environments, the dipoles orientate in bands of positive and negative PV. Similar bands are known to initiate secondary wave development (e.g. Parker, 1998). Further research should find out how the diabatically generated dipoles influence the larger-scale flow. A more sophisticated tracking method (e.g. an object-based one) might be necessary, since the PV dipoles are generally larger in size than the associated updraughts. Moreover, splitting and merging of anomalies should be treated in a more sophisticated way.

It is interesting to examine how the general morphology of convective cells changes with model resolution. One could apply the tracking and compositing algorithm to models with a higher resolution. The size of the convective cells is generally too large in a model with a grid spacing of a few km (e.g. Stein *et al.*, 2015); decreasing the grid spacing below 1 km can improve this. The convective cells initiated in a model with a higher resolution are therefore expected to be more physically realistic.

One could further investigate if PV could be used in the data reduction problem. Prior research has shown that the inclusion of physical correlations in post-processing methods improves the exploitation of the available forecast information (e.g. Röpnack *et al.*, 2013; Keune *et al.*, 2014). Most physically based post-processing methods are only two-dimensional, e.g. for wind speed (Schuhen *et al.*, 2012), or wind speed and temperature (Baran and Möller, 2015). PV holds dynamical and thermodynamical information in one variable. The coherent PV anomalies suggest, together with the linear model used by Chagnon and Gray (2009), that a significant data reduction might be possible. One approach might using vertical normal modes (VNM), as in Renkl (2013). One could compare this with ensemble copula coupling (ECC), which also preserves physical and spatial correlations between variables (Schefzik *et al.*, 2013), and which is relatively easy to apply on a large dataset.

Acknowledgements

This research was carried out in the WEX-MOP project, which is supported by the Volkswagen Foundation. The COSMO-DE model used in this study was kindly provided by the DWD. The authors also thank the reviewers for their useful comments which helped to improve the manuscript.

Supporting information

The following supporting information is available as part of the online article:

Figure S1. Cross-sections of PV (coloured contours) and w (contour lines) along the zero y-axis of Figure 8. Different times indicated at the top of each panel indicated the time since the maximum (Gaussian filtered) vertical velocity.

Figure S2. As Figure S1, but now for the 10% strongest PV cells. Note the different colour bar used.

Figure S3. As Figure S1, but now for the cells with the 10% strongest precipitation rates. Note the different colour bar used.

References

Aebischer U, Schär C. 1998. Low-level potential vorticity and cyclogenesis to the lee of the Alps. *J. Atmos. Sci.* **55**: 186–207. https://doi.org/10.1175/1520-0469(1998)055<0186:llpvac>2.0.CO;2.

Appenzeller C, Davies HC. 1996. PV morphology of a frontal-wave development. *Meteorol. Atmos. Phys.* **58**: 21–40. https://doi.org/10.1007/BF01027554.

Arnaud Y, Desbois M, Maizi J. 1992. Automatic tracking and characterization of African convective systems on Meteosat pictures. *J. Appl. Meteorol.* **31**: 443–453. https://doi.org/10.1175/1520-0450(1992)031<0443:atacoa>2.0.CO;2.

Baldauf M, Seifert A, Förstner J, Majewski D, Raschendorfer M, Reinhardt T. 2011. Operational convective-scale numerical weather prediction with the COSMO model: Description and sensitivities. *Mon. Weather Rev.* **139**: 3887–3905.

Baran S, Möller A. 2015. Joint probabilistic forecasting of wind speed and temperature using Bayesian model averaging. *Environmetrics* **26**: 120–132. https://doi.org/10.1002/env.2316.

Caine S, Lane TP, May PT, Jakob C, Siems ST, Manton MJ, Pinto J. 2013. Statistical assessment of tropical convection-permitting model simulations using a cell-tracking algorithm. *Mon. Weather Rev.* **141**: 557–580.

Chagnon JM, Bannon PR. 2005. Wave response during hydrostatic and geostrophic adjustment. Part I: Transient dynamics. *J. Atmos. Sci.* **62**: 1311–1329.

Chagnon JM, Gray SL. 2009. Horizontal potential vorticity dipoles on the convective storm scale. *Q. J. R. Meteorol. Soc.* **135**: 1392–1408.

Chagnon JM, Gray SL, Methven J. 2012. Diabatic processes modifying potential vorticity in a North Atlantic cyclone. *Q. J. R. Meteorol. Soc.* **139**: 1270–1282. https://doi.org/10.1002/qj.2037.

Clark A, Bullock R. 2014. Application of object-based time-domain diagnostics for tracking precipitation systems in convection-allowing models. *Weather and Forecasting* **29**: 517–542.

Conzemius RJ, Montgomery MT. 2009. Clarification on the generation of absolute and potential vorticity in mesoscale convective vortices. *Atmos. Chem. Phys.* **9**: 7591–7605.

Cram TA, Montgomery MT. 2002. Early evolution of vertical vorticity in a numerically simulated idealized convective line. *J. Atmos. Sci.* **59**: 2113–2127.

Dacre HF, Gray SL. 2009. The spatial distribution and evolution characteristics of North Atlantic cyclones. *Mon. Weather Rev.* **137**: 99–115. https://doi.org/10.1175/2008MWR2491.1.

Davies-Jones R. 1984. Streamwise vorticity: The origin of updraft rotation in supercell storms. *J. Atmos. Sci.* **41**: 2991–3006.

Davis CA, Weisman ML. 1994. Balanced dynamics of mesoscale vortices produced in simulated convective systems. *J. Atmos. Sci.* **51**: 2005–2030.

Dixon M, Wiener G. 1993. TITAN: Thunderstorm identification, tracking, analysis, and nowcasting–a radar-based methodology. *J. Atmos. Oceanic Technol.* **10**: 785–797. https://doi.org/10.1175/1520-0426(1993)010<0785:ttitaa>2.0.CO;2.

Droegemeier KK, Lazarus SM, Davies-Jones R. 1993. The influence of helicity on numerically simulated convective storms. *Mon. Weather Rev.* **121**: 2005–2029.

Emanuel KA. 1994. *Atmospheric Convection*. Oxford University Press: Oxford, UK.

Evensen G. 1994. Sequential data assimilation with a nonlinear quasi-geostrophic model using Monte Carlo methods to forecast error statistics. *J. Geophys. Res. Oceans* **99**: 10143–10162. https://doi.org/10.1029/94JC00572.

Grams CM, Wernli H, Böttcher M, Čampa J, Corsmeier U, Jones SC, Keller JH, Lenz CJJ, Wiegand L. 2011. The key role of diabatic processes in modifying the upper-tropospheric wave guide: A North Atlantic case-study. *Q. J. R. Meteorol. Soc.* **137**: 2174–2193. https://doi.org/10.1002/qj.891.

Groenemeijer PH, van Delden A. 2007. Sounding-derived parameters associated with large hail and tornadoes in the Netherlands. *Atmos. Res.* **83**: 473–487.

Hakim GJ. 2008. A probabilistic theory for balance dynamics. *J. Atmos. Sci.* **65**: 2949–2960.

Hakim G, Torn R. 2008. Ensemble Synoptic Analysis. *Meteorol. Monogr.* **55**: 147–162. https://doi.org/10.1175/0065-9401-33.55.147.

Han L, Fu S, Zhao L, Zheng Y, Wang H, Lin Y. 2009. 3D convective storm identification, tracking, and forecasting –an enhanced TITAN algorithm. *J. Atmos. Oceanic Technol.* **26**: 719–732.

Haynes PH, McIntyre ME. 1987. On the evolution of vorticity and potential vorticity in the presence of diabatic heating or other forces. *J. Atmos. Sci.* **44**: 828–841.

Holton JR. 2004. *An Introduction to Dynamic Meteorology* (4th edn). Elsevier Academic Press: Amsterdam, Netherlands.

Hoskins BJ. 1997. A potential vorticity view of synoptic development. *Meteorol. Appl.* **4**: 325–334.

Hoskins BJ, McIntyre ME, Robertson AW. 1985. On the use and significance of isentropic potential vorticity maps. *Q. J. R. Meteorol. Soc.* **111**: 877–946. https://doi.org/10.1002/qj.49711147002.

Johnson JT, MacKeen PL, Witt A, Mitchell EDW, Stumpf GJ, Eilts MD, Thomas KW. 1998. The storm cell identification and tracking algorithm: An enhanced WSR-88D algorithm. *Weather and Forecasting* **13**: 263–276. https://doi.org/10.1175/1520-0434(1998)013<0263:tsciat>2.0.CO;2.

Keune J, Ohlwein C, Hense A. 2014. Multivariate probabilistic analysis and predictability of medium-range ensemble weather forecasts. *Mon. Weather Rev.* **142**: 4074–4090. https://doi.org/10.1175/MWR-D-14-00015.1.

Kyznarová H, Novák P. 2009. CELLTRACK – convective cell tracking algorithm and its use for deriving life cycle characteristics. *Atmos. Res.* **93**: 317–327.

Lilly DK. 1986. The structure, energetics and propagation of rotating convective storms. Part I: Energy exchange with the mean flow. *J. Atmos. Sci.* **43**: 113–125.

Limbach S, Schömer E, Wernli H. 2012. Detection, tracking and event localization of jet stream features in 4-D atmospheric data. *Geosci. Model Dev.* **5**: 457–470.

McCaul EW Jr., Weisman ML. 2001. The sensitivity of simulated supercell structure and intensity to variations in the shapes of environmental buoyancy and shear profiles. *Mon. Weather Rev.* **129**: 664–687.

Malardel S, Joly A, Courbet F, Courtier P. 1993. Nonlinear evolution of ordinary frontal waves induced by low-level potential vorticity anomalies. *Q. J. R. Meteorol. Soc.* **119**: 681–713.

Mills E. 2005. Insurance in a climate of change. *Science* **309**: 1040–1044.

Moseley C, Berg P, Haerter J. 2013. Probing the precipitation life cycle by iterative rain cell tracking. *J. Geophys. Res. Atmos.* **118**: 13–361. https://doi.org/10.1002/2013JD020868.

Moseley C, Hohenegger C, Berg P, Haerter JO. 2016. Intensification of convective extremes driven by cloud–cloud interaction. *Nat. Geosci.* **9**: 748–752. https://doi.org/10.1038/ngeo2789.

Murray RJ, Simmonds I. 1991. A numerical scheme for tracking cyclone centres from digital data. Part I: Development and operation of the scheme. *Aust. Meteorol. Mag.* **39**: 155–166.

Parker DJ. 1998. Secondary frontal waves in the North Atlantic region: A dynamical perspective of current ideas. *Q. J. R. Meteorol. Soc.* **124**: 829–856.

Pinto JG, Spangehl T, Ulbrich U, Speth P. 2005. Sensitivities of a cyclone detection and tracking algorithm: Individual tracks and climatology. *Meteorol. Z.* **14**: 823–838.

Plant RS. 2008. Statistical properties of cloud lifecycles in cloud-resolving models. *Atmos. Chem. Phys. Discuss.* **8**: 20537–20564. https://doi.org/10.5194/acpd-8-20537-2008.

Raymond DJ, Jiang H. 1990. A theory of long-lived mesoscale convective systems. *J. Atmos. Sci.* **47**: 3067–3077.

Renkl C. 2013. 'The vertical structure of the atmosphere in COSMO-DE-EPS: Multivariate ensemble postprocessing in the space of vertical normal modes', Master thesis, University of Bonn: Bonn, Germany.

Romero R, Gayà M, Doswell CA. 2007. European climatology of severe convective storm environmental parameters: A test for significant tornado events. *Atmos. Res.* **83**: 389–404.

Röpnack A, Hense A, Gebhardt C, Majewski D. 2013. Bayesian model verification of NWP ensemble forecasts. *Mon. Weather Rev.* **141**: 375–387.

Rudeva I, Gulev SK. 2007. Climatology of cyclone size characteristics and their changes during the cyclone life cycle. *Mon. Weather Rev.* **135**: 2568–2587.

Schär C, Sprenger M, Lüthi D, Jiang Q, Smith RB, Benoit R. 2003. Structure and dynamics of an Alpine potential-vorticity banner. *Q. J. R. Meteorol. Soc.* **129**: 825–855. https://doi.org/10.1256/qj.02.47.

Schättler U, Doms G, Schraff C. 2014. 'A description of the nonhydrostatic regional COSMO-model, Part VII: User's guide'. http://www.cosmo-model.org (accessed 31 January 2017).

Schefzik R, Thorarinsdottir TL, Gneiting T. 2013. Uncertainty quantification in complex simulation models using ensemble copula coupling. *Stat. Sci.* **28**: 616–640.

Schuhen N, Thorarinsdottir TL, Gneiting T. 2012. Ensemble model output statistics for wind vectors. *Mon. Weather Rev.* **140**: 3204–3219. https://doi.org/10.1175/MWR-D-12-00028.1.

Schumacher RS, Johnson RH. 2008. Mesoscale processes contributing to extreme rainfall in a midlatitude warm-season flash flood. *Mon. Weather Rev.* **136**: 3964–3986. https://doi.org/10.1175/2008MWR2471.1.

Shapiro MA, Thorpe AJ. 2004. THORPEX international science plan. WMO TD No 1246. World Meteorological Organization: Geneva, Switzerland.

Stein THM, Hogan RJ, Clark PA, Halliwell CE, Hanley KE, Lean HW, Nicol JC, Plant RS. 2015. The DYMECS project: a statistical approach for the evaluation of convective storms in high-resolution NWP models. *Bull. Am. Meteorol. Soc.* **96**: 939–951. https://doi.org/10.1175/BAMS-D-13-00279.1.

Thompson RL, Edwards R, Hart JA, Elmore KL, Markowski P. 2003. Close proximity soundings within supercell environments obtained from the rapid update cycle. *Weather and Forecasting* **18**: 1243–1261. https://doi.org/10.1175/1520-0434(2003)018<1243:cpswse>2.0.CO;2.

Thompson RL, Mead CM, Edwards R. 2007. Effective storm-relative helicity and bulk shear in supercell thunderstorm environments. *Weather and Forecasting* **22**: 102–115. https://doi.org/10.1175/WAF969.1.

von Storch H, Zwiers FW. 1988. Recurrence analysis of climate sensitivity experiments. *J. Clim.* **1**: 157–171.

Viúdez Á, Dritschel DG. 2004. Optimal potential vorticity balance of geophysical flows. *J. Fluid Mech.* **521**: 343–352. https://doi.org/10.1017/S0022112004002058.

Weijenborg C, Friederichs P, Hense A. 2015. Organisation of potential vorticity on the mesoscale during deep moist convection. *Tellus A* **67**: 25705. https://doi.org/10.3402/tellusa.v67.25705.

Weisman M, Klemp J. 1982. The dependence of numerically simulated convective storms on vertical wind shear and buoyancy. *Mon. Weather Rev.* **110**: 504–520.

Weisman ML, Klemp JB. 1984. The structure and classification of numerically simulated convective stormsin directionally varying wind shears. *Mon. Weather Rev.* **112**: 2479–2498. https://doi.org/10.1175/1520-0493(1984)112<2479:tsacon>2.0.CO;2.

Zhang X, Walsh JE, Zhang J, Bhatt US, Ikeda M. 2004. Climatology and interannual variability of Arctic cyclone activity: 1948–2002. *J. Clim.* **17**: 2300–2317.